ACS OMEGA

http://pubs.acs.org/journal/acsodf

Article

Optimizing the Ultrashort Laser Pulses for In Situ Nanostructure Generation Technique for High-Performance Supercapacitor Electrodes Using Artificial Neural Networks and Simulated Annealing Algorithms

Kavian Khosravinia and Amirkianoosh Kiani*

Cite This: *ACS Omega* 2023, 8, 17220−17233

Read Online

ACCESS | Metrics & More | Article Recommendations

ABSTRACT: Transition metals (TMs) are being investigated as electrodes for pseudocapacitors, where an oxide layer is necessary to allow for rapid redox reactions. In this work, we utilized an in situ, rapid, binder-free, and green method for the fast fabrication of pseudocapacitor electrodes called ultrashort laser pulses for in situ nanostructure generation (ULPING) to form oxide layers on a titanium sheet. By utilizing this fabrication technique on a titanium sheet, a specific areal capacitance of 0.3579 mF cm^{-2} was achieved at a current density of 0.25 mA cm^{-2}. However, the laser fabrication parameters were selected experimentally and resulted in low performance of pseudocapacitors. Therefore, one of the main objectives of this study was to find the optimal laser fabrication parameters to achieve the highest specific areal capacitance. A large dataset was generated to find the relationship between the laser fabrication parameters and the electrochemical behavior performance (impedance and specific areal capacitance) of the fabricated electrodes by using an artificial neural network (ANN). We used an optimization algorithm (simulated annealing-SA) to overlook the trained ANN model as a black box and try to maximize the objective function, which in our case is a specific capacitance value, to find the most optimal laser fabrication parameters. Using SA, optimal laser fabrication parameters were found, which increased the specific areal capacitance to 0.9999 mF cm^{-2} at a current density of 0.25 mA cm^{-2}. The results demonstrated that the conducted study has the potential to introduce effective techniques for utilizing ULPING to produce nanoscale structures on TMs. These structures have the potential to be employed as electrodes in pseudocapacitors. Additionally, the research underscores the significance of employing data-driven approaches in electrode design procedures.

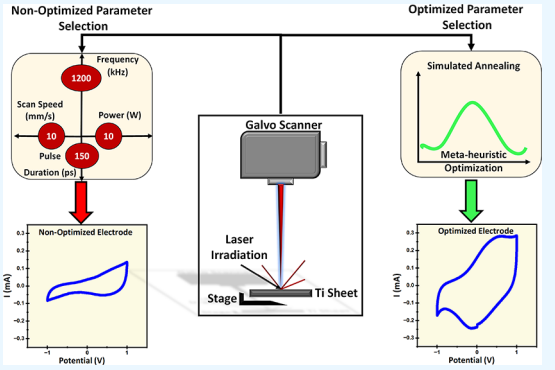

INTRODUCTION

The implementation of renewable energy systems is contingent upon the availability of efficient energy storage devices.[1] The high-power density of supercapacitors enables them to store and release energy quickly, making them a viable option for various applications, including regenerative brakes, elevators, and electric trains. Their ability to charge and discharge rapidly allows for efficient energy management in these systems.[2,3] Despite the excellent performance of carbon-based supercapacitors in real-world applications, their low capacitance and poor conductivity render them unsuitable for next-generation technologies.[4−6] Pseudocapacitors with transition metal (TM)-based electrodes have emerged as a more promising solution as they exhibit superior performance compared to carbon-based supercapacitors.[7−9] These devices feature electrodes comprising redox materials that enable Faradaic reactions and fast charging/discharging kinetics, resulting in higher power density and charging rate than lithium-ion batteries.[10,11] Although TM-based electrodes in pseudocapacitors exhibit superior electrochemical performance, the major challenge lies in their synthesis method. Typical methods like chemical vapor deposition, solvothermal synthesis, physical vapor deposition, and hydrothermal synthesis necessitate prolonged processes at elevated thermal budgets and yield restricted controllability and suboptimal results.[12−14] Synthesis of active material for charge storage, for example, currently takes between 24 and 48 h. Thus, the challenge remains to develop a cost-effective and scalable synthesis of pseudocapacitors with TM-based electrodes.

Received: March 13, 2023
Accepted: April 19, 2023
Published: May 3, 2023

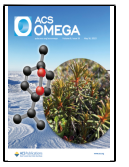

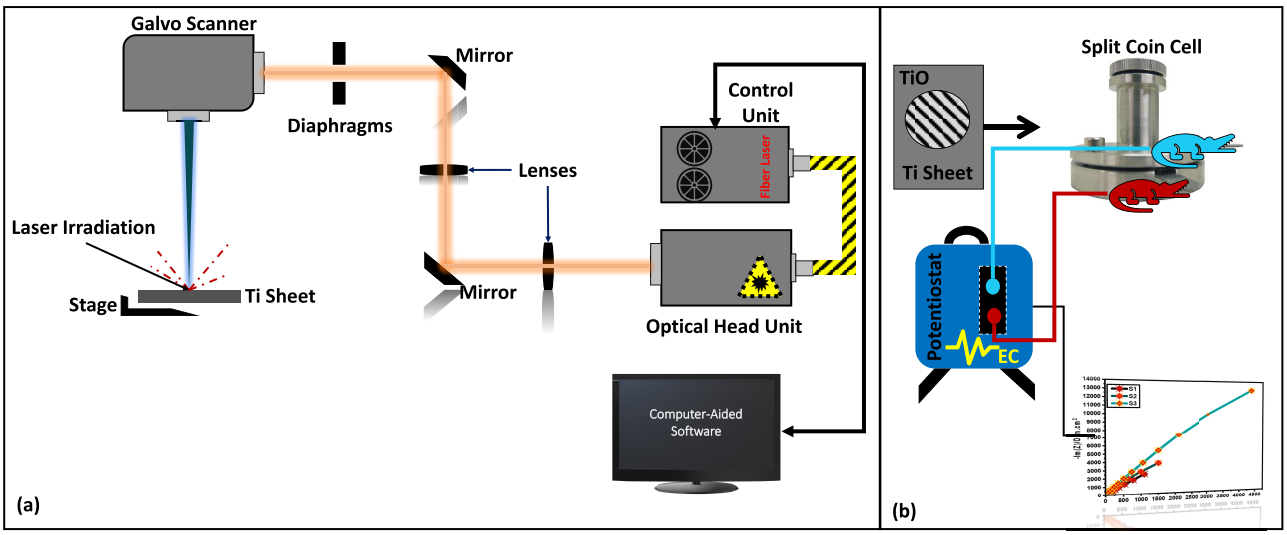

Figure 1. Schematic diagram of the experimental setup for the formation of a TiO layer through laser irradiation. (a) Laser parameters can be modified using computer-aided software (Marking Mate 2.7), and laser irradiation is performed by fine-tuning and adjusting all the apparatus for effective and efficient fabrication. (b) The two coin-cell setup was utilized for analysis, and electrochemical tests were performed using a potentiostat.

Consequently, to overcome the fabrication challenge, we previously introduced an advanced approach known as ultrashort laser pulses for in situ nanostructure generation (ULPING).[15−18] This green synthesis approach is highly controllable and produces enhanced pseudocapacitor electrodes in a single step. Unlike traditional methods, which generate separate byproducts, ULPING results in in situ substrate modification.[19,20] Moreover, computer-aided design can be employed to precisely control the laser processing approach, enabling adjustments to various parameters such as power, pulse repetition rate, frequency, scan speed, and specific pattern formation. This level of control enhances the accuracy and reproducibility of the laser processing method.

Transition metals (TMs) are being studied as pseudocapacitor electrodes, where an oxide layer is required to allow for fast redox reactions.[21−23] Recently, our research group used direct ULPING to generate oxide layers (NiO and TiO) on Ni and Ti metal sheets under ambient settings using varied laser parameters. The research concentrated on irradiating Ti metal sheets with ULPING, which resulted in the formation of titania 3D nanonetworks (T3DN).[15,18] Comparing the laser-treated surface to a control surface without treatment, it was observed that two laser treatments increased the areal capacitance to 6.91 mF cm^{-2}. The formation of self-grown 3D nanostructures occurs through a series of ultrafast events during ULPING, which is triggered by electromagnetic radiation pulses on the target material's surface. Recently, we conducted a study on the impact of scan speed and frequency on the formation of NiO through ULPING.[17] Our results showed that while frequency is a crucial factor, adjusting the scan speed of the laser beam can also lead to improvements. The optimal scan speed was determined to be 10 mm s^{-1}, as it allowed for better nanostructure generation and increased phase transformation of Ni into NiO. The results also indicated an areal capacitance of 93 mF/cm^2 when a discharge current of 1 mA/cm^2 was applied under these specific conditions.

The outcomes of both investigations exhibited the originality, straightforwardness, and efficacy of the ULPING technique in producing capable electrode materials for pseudocapacitors.[18] The surfaces activated by ULPING were free of binders, generated in a solitary step, and did not require the use of chemicals.[18] It is evident that the laser input parameters exerted a considerable influence on the electrochemical effectiveness of the pseudocapacitor. Despite our confidence in the efficiency, user-friendliness, and cost-effectiveness of the ULPING technique, we acknowledge the need for further improvement, especially in the laser parameter selection strategy. Nevertheless, in our latest research, we have employed machine learning (ML) techniques to establish a theoretical validation of the correlation between laser input parameters and the electrochemical performance of pseudocapacitors.[18] We constructed various ML algorithms, including artificial neural network (ANN), Gaussian process regression (GPR), and random forest (RF), and identified a relationship between the electrochemical behavior performance, including specific areal capacitance and impedance, and the laser input parameters.[18] In all prior studies, we determined the laser parameters through experimentation and basing on the material type. However, a crucial question arises: What if an operational strategy for parameter selection is provided, which optimizes the laser parameters and enhances the electrochemical performance of the pseudocapacitor? Hence, an investigation into the connection between laser parameters and the material properties of the generated nanostructures is warranted. By utilizing ML methods, valuable insights can be gained on this front. Therefore, developing and executing an optimization algorithm could aid in identifying the optimal laser parameters for the most efficient electrode production. Given the potential applications of ULPING in the pseudocapacitor industry, further research is imperative to address these queries.

This paper details the progress made by our research group in the manufacturing of electrodes using ULPING on Ti sheets and the utilization of a customized ANN-Enabled optimization technique for enhancing electrochemical behavior of pseudocapacitors electrode through two phases. In the first phase, 31 electrodes with distinct T3DN structural characteristics were fabricated by varying 31 different laser parameters, including frequency, power, pulse duration, and scanning speed. These electrodes were used to prototype 496-coin cells, with each electrode paired individually to create a mix-and-match matrix.[18]

https://doi.org/10.1021/acsomega.3c01676
ACS Omega 2023, 8, 17220−17233

To investigate the effect of laser parameter variation on T3DN properties, the prototyped coin cells were analyzed through various characterization techniques, such as scanning electron microscopy (SEM), energy-dispersive spectroscopy (EDS), X-ray photoelectron spectroscopy (XPS), and X-ray diffraction (XRD). The electrochemical behavior of the coin cells was studied using a potentiostat and different analyses, including cyclic voltammetry (CV), galvanostatic charge−discharge (GCD), and electrochemical impedance spectroscopy (EIS). In the second phase of our study, we employed and customized the ANN model that we developed in our previous work to make it suitable for fitting in the optimization problem.[18] We used the customized ANN model to analyze a large dataset gathered from the experiments and study the correlation between fabrication variables and pseudocapacitor performance indicators. First, we used the trained customized ANN model to predict the electrochemical behavior of pseudocapacitors, including specific capacitance and internal impedance. Then, we applied a simulated annealing (SA) optimization algorithm to utilize the trained customized ANN model as a black box and maximize the objective function, which, in our case, was a specific capacitance value. This enabled us to identify the most optimal laser fabrication parameters. The results of this study suggest that ULPING could be a promising method for generating nanostructures on TMs for pseudocapacitor electrodes.

EXPERIMENTAL PROCEDURES AND PROTOCOLS

Material Synthesis and Electrode Preparation Using the ULPING Technique. The experiment utilized a commercial grade 4 titanium sample with a thickness of 0.2 mm that underwent polishing and cleaning procedures using acetone and DI water. The ULPING technique was employed by exposing the sample to ambient atmospheric conditions without elaborate shielding, and a 150 ps laser pulse system was used to perform pulse ionization at a constant wavelength of 1060 nm (IPG Laser Model: YLPP-1-150 V-30) (see Figure 1a). The laser beam diameter was reduced to 6 mm and focused on an XY galvanometer scanner to achieve a theoretical laser spot diameter of 20 μm using an F-theta lens with specified parameters.[18] Laser patterning parameters such as scanning speed and pitch were determined using the CAD software Marking Mate 2.7.[18] The experiment involved the fabrication of 31 distinct electrodes using a constant pitch pattern and varying parameters such as laser power, frequency, pulse duration, and scan speed.[18]

Specifically, the laser power ranged from 5 to 20 W, frequency ranged from 30 to 1200 kHz, pulse duration varied from 150 ps to 5 ns, and scan speed ranged from 5 to 500 mm s^{-1}.

The pitch refers to the distance between two consecutive lines created by the laser beam. The samples, which were punched into 6 mm diameter discs containing TiO as the active material with a surface area of 27.2 mm^2, were then subjected to laser irradiation.[18] A summary of the distinct laser parameters used for each sample can be found in Table 1. The accuracy of the IPG Laser in terms of power, frequency, and scan speed can be influenced by environmental conditions. IPG Photonics provides specifications for the laser that describe its performance and accuracy under specific conditions. The specifications detail the expected accuracy of the laser's power, frequency, and scan speed when environmental conditions are ideal. In our experiments, however, the laser procedure for fabricating each electrode took between 5 and 10 min, indicating that no errors occurred.

Table 1. Laser Parameters for Different Samples

laser parameters	variation	range/style	errors
power	varied	5−20 W	±3% over 8 h
frequency	varied	30−1200 kHz	±10 kHz over 8 h
pulse duration	varied	150 ps−5 ns	±5% over 8 h
scan speed	varied	5−500 mm/s	±0.5 mm/s over 8 h
pitch	constant	arrow sequence	NA

Characterizing Materials and Structures. The samples were examined using SEM at both high and low magnifications to investigate their morphology. EDX was used to analyze the elemental composition of the samples, with particular emphasis on identifying Ti and O. XPS was employed to study the oxidation states and phases of TiO on the surface of the laser-irradiated structure. XRD was also conducted to analyze the diffraction pattern and crystalline structure of the electrodes. Furthermore, the porosity of the fabricated electrode area was determined using ImageJ 1.53 software.[24]

Measurement of Electrochemical Properties. A two-electrode configuration (coin cell) setup was used for the electrochemical study, with two symmetrical coin-shaped electrodes separated by a separator saturated with sodium sulfate (Na_2SO_4) electrolyte (see Figure 1b). The study involved various experiments, including CV, GCD, and EIS, conducted using a SP-150 Potentiostat.[18] CV measurements were executed with scan rates of 500 mV/s (with a consistent potential range of −1 to 1 V) and 50 mV/s (with a constant potential range of −0.8 to 0.8 V), while the EIS measurements were taken with a perturbation voltage of 50 mV/s across frequencies ranging from 100 mHz to 100 kHz[18]. GCD experiments were performed at potentials ranging from −0.8 to 0.8 V and current densities from 0.25 mA/cm^2. These tests were performed to assess the effectiveness of the fabrication method that utilized laser irradiation and ablation to create the oxide layer.[18]

Statistical Analysis. Three electrodes were made for each group of samples to ensure accurate data processing, and all experiments were done in triplicate. The mean value was calculated from the resulting data. Geometric metrics such as fibers and porosity were determined by examining SEM pictures in ImageJ software with an estimated error rate of 5% (developed by Wayne Rasband at the National Institutes of Health in the USA).[24]

MODELING AND OPTIMIZATION OF FABRICATION STRATEGIES FOR PSEUDOCAPACITOR ELECTRODES

From a theoretical perspective, ML is considered a valuable tool for predicting properties and designing materials for supercapacitors.[25,26] In the literature, several ML algorithms have been used for predicting supercapacitor performance metrics, with ANNs demonstrating superior prediction accuracy compared to other algorithms.[27,28] For example, Jha et al.[28] used an ANN to predict the performance of an alkali lignin-based flexible supercapacitor, demonstrating that ANNs had the highest predictive accuracy and excellent robustness compared to other ML algorithms. Similarly, in our previous work, we also employed ANN to predict the properties of pseudocapacitors and achieved favorable results.[18] Although theoretical modeling and ML algorithms are useful for predicting the performance of supercapacitors, the optimal electrode design cannot be achieved solely through these methods from a manufacturing perspective. This is the juncture at which the key leverage in ML

https://doi.org/10.1021/acsomega.3c01676
ACS Omega 2023, 8, 17220−17233

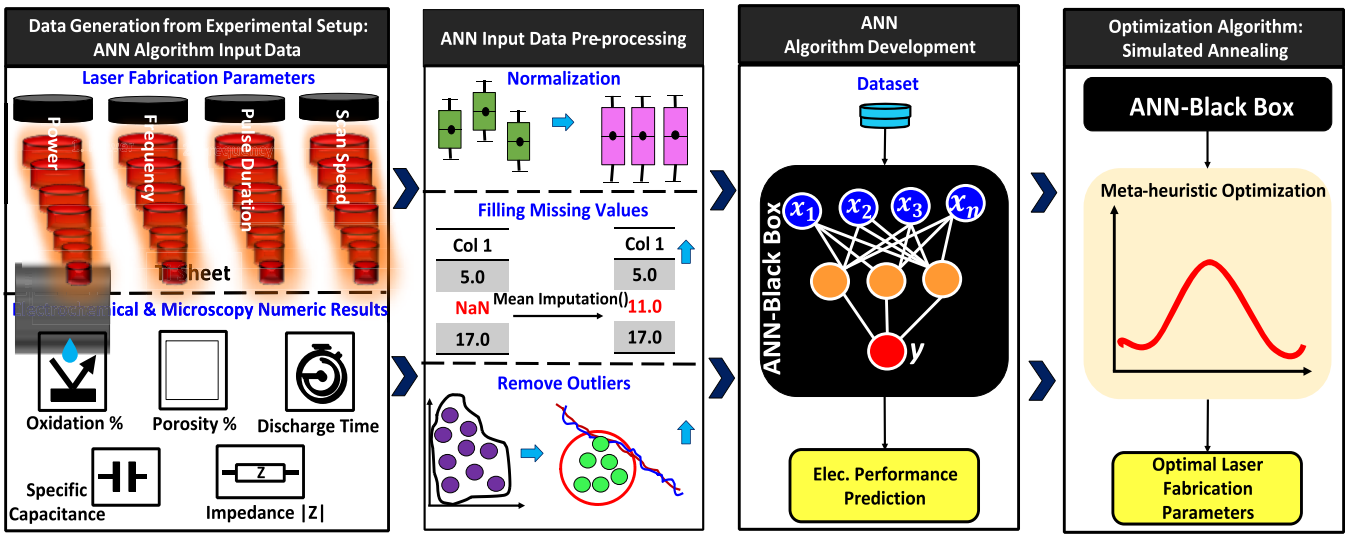

Figure 2. Modeling and optimization process consist of four stages. Stage 1: this involves the generation of a comprehensive dataset from the experimental setup, which includes information on laser fabrication parameters and results of electrochemical and microscopy analysis. Stage 2: the generated dataset is structured and prepared for the next stage. Stage 3: ANN is built and trained on the dataset to forecast electrochemical performance measures, such as impedance and specific areal capacitance, of pseudocapacitors. Stage 4: the trained ANN is employed in a meta-heuristic optimization algorithm to identify the optimal laser fabrication parameters.

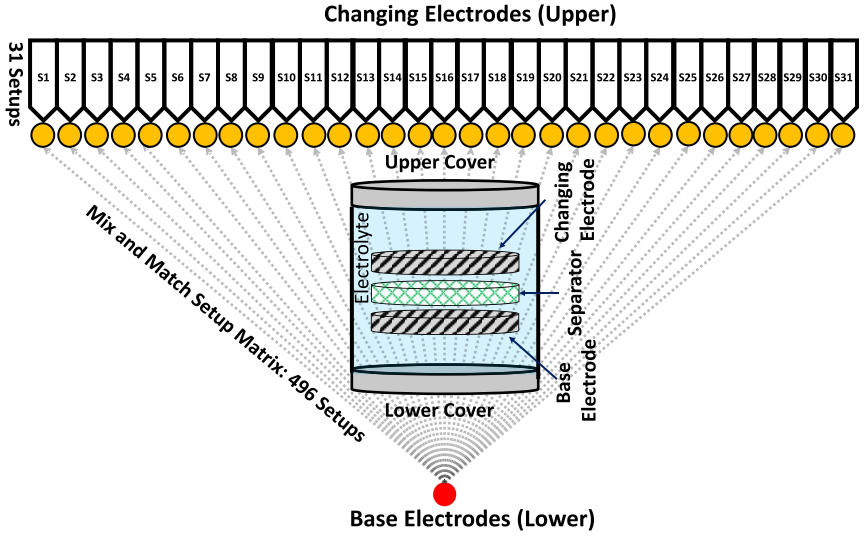

Figure 3. To generate data from the experimental setup, a unique testing matrix known as the mix-and-match testing matrix is established. This matrix involves the evaluation of 31 prepared electrodes, where each electrode is subjected to individual testing against itself and the other electrodes.

approaches, optimization, enters the game of optimal electrode design. In our study, we fabricated numerous electrodes using the ULPING technique, making it difficult to predict the optimal fabrication parameters without using an optimization algorithm. Therefore, the main goal of this section is to customize an ANN model that can be fit into an optimization algorithm to achieve the optimal electrode design. The aim of this section is to accomplish four objectives as shown Figure 2. The first objective is to generate a dataset from the experimental setup. The second objective is to clean and prepare the generated dataset for use in an ANN model. The third objective entails using the prepared dataset to train an ANN model for forecasting the electrochemical behavior of laser-treated pseudocapacitors. The final objective is to incorporate a meta-heuristic optimization algorithm (simulated annealing-SA), utilizing the trained ANN model, to determine the most optimal laser fabrication parameters. The dataset generation and preparation, the development of the model, and the optimization process are separated into four stages, as depicted in Figure 2.

Data Generation from the Experimental Setup. In previous work, we provided a method for generating large datasets for ML algorithms.[18] We will explain this method briefly because it is one of the fundamental pillars of this study. To accomplish this, we developed a unique mix-and-match testing matrix, as depicted in Figure 3. This matrix was designed to be simple and straightforward, where for the first coin cell setup, we used 1 M salt as the electrolyte solution and positioned sample 1 (S1-base electrode) in the lower cover of the MTI coin cell setup, with the same S1 electrode located on top of it. This process was repeated 31 times, with the S1 electrode serving as the base and the other top electrode serving as the changing electrode.[18] We also tested the S2 electrode 30 times with itself and other electrodes, except for S1, which was tested in the previous round. Finally, we repeated the testing process 31

https://doi.org/10.1021/acsomega.3c01676
ACS Omega 2023, 8, 17220−17233

times, with each electrode serving as the base and top electrode at different times. This resulted in a total of 496 electrode sets, which were assembled and subjected to consistent CV, GCD, and EIS setup configurations.[18] Our aim was to generate a large and diverse dataset that can be used to train and validate ML models for better performance and prediction accuracy.

ANN Algorithm Input Data. Various quantitative values were measured and categorized into two groups: numeric results obtained from microscopy and electrochemical analysis and laser fabrication parameters.[18] Laser fabrication parameters such as power (W), frequency (kHz), pulse duration (ps−ns), and scan speed (mm s^{-1}) were recorded for both the base and changing electrodes.[18] Multiple variables such as discharge time (seconds), specific areal capacitance (mF/cm^2), and capacity (mA h) are obtained from the electrochemical analysis. Moreover, the impedance (Ohm), phase angle (|Z|-degree°), and real impedance (Ohm) are recorded at lower and higher frequencies.[18]

It is important to mention that the specific areal capacitance of each sample can be computed from the GCD curve using the following equation[2,29];

$$C_A = \frac{J \times \Delta t}{\Delta V}, \text{ where } J = \frac{i}{A} \quad (1)$$

where J is the areal current density (0.25 mA cm^{-2}), Δt is the discharge time from fully charged (0.8 V) to fully discharged (−0.8 V), and ΔV is the stable potential window.[18]

Numerical parameters, including oxidation percentage (%), Ti/oxidation ratio (%), and porosity percentage (%), were obtained through microscopy analysis of both the base and changing electrodes. The ImageJ software was utilized to conduct morphological analysis of the laser-treated pseudocapacitor electrodes. The scanning electron microscope (SEM) images of the ablated surfaces were analyzed to identify the topological features. The porosity of each sample was calculated by adjusting the SEM image threshold until the porous structure was emphasized. The collected data constitutes the final raw dataset from the experimental setup and is suitable for additional processing to be used in the ANN model.

ANN Input Data Preprocessing. The preprocessing of data is an essential step in the construction of ANN models. This process involves the manipulation of raw data (experimental data) into a format that is more easily interpretable and compatible with the neural network algorithm. The primary procedures in data preprocessing for ANN modeling are data cleaning and transformation, removal of outliers, handling of missing data, and data normalization (see Figure 2). The objective of these procedures is to ensure that the data is properly prepared and optimized for use in the neural network, resulting in a more accurate and efficient model.[30,31]

Outlier Removal and Missing Value Imputation. As previously discussed in the statistical analysis section, in order to ensure accurate data processing, three electrodes were fabricated for each group of samples, and all experiments were performed in triplicate. However, some data points in the final dataset were found to be significantly different from other data points, potentially due to measurement errors or other factors that can occur during experimental work. These data points are known as outliers. The process of removing outliers involves identifying and eliminating data points that are considered to be outliers. This can be accomplished manually by visually inspecting the data or by using statistical techniques such as the interquartile range (IQR).[32] IQR is calculated from the first (Q_1) and third (Q_3) quartiles and represents the width of the box in a box-and-whisker plot. Data points (X_i) that fall outside the IQR are defined as outliers. In this study, the dataset was first sorted in ascending order, and Q_1 and Q_3 were calculated as the values that are greater than 25% and 75% of the data points, respectively. The IQR was then calculated as the difference between Q_3 and Q_1, IQR = $Q_3 - Q_1$. Data points that lie beyond the typical data range or have a low likelihood of occurrence were deleted from the raw dataset.

In data analysis, it is common to encounter missing values in datasets due to various reasons such as errors in data collection or entry. These missing values can be problematic and need to be handled appropriately. One popular method to address missing values is called mean imputation, which involves replacing the missing values with the mean value of the variable across all the other observations in the dataset.[33] In our analysis, we observed a few missing values and addressed them using mean imputation, as shown in Figure 2.

Data Normalization. Data normalization is a critical aspect of data preprocessing that can enhance the performance of machine learning models. It aims to transform data into a standard scale to ensure each feature contributes equally to the analysis. Normalization can also accelerate the convergence speed and minimize negative impacts.[18] To normalize the input dataset in this study, we employed min−max scaling technique, which scales the feature values to a range of [−1, 1] by subtracting the minimum value and dividing it by the range of values. The formula used for min−max scaling is[34]

$$x' = \frac{(x - x_{\min})}{x_{\max} - x_{\min}} \quad (2)$$

where x is the original value of the feature, $x_{\min}$ is the minimum value of the feature, $x_{\max}$ is the maximum value of the feature, and x' is the normalized value of the feature.

Data Partitioning for Model Training and Evaluation. In machine learning, it is common practice to divide a dataset into a training set and a testing set. The training set is used to train the model, while the testing set is used to evaluate the model's performance on data it has not seen before. In this study, the dataset was randomly split into 80% training data and 20% testing data, with 370 cycles used for training and the remaining cycles used for testing.[18] However, our dataset is small, so this approach may not provide an accurate evaluation of the model's performance. To address this issue, k-fold cross-validation (CV) was employed. This involves dividing the dataset into k equally sized folds, where each fold serves as the testing set at some point. For example, if k is set to 10, the dataset is divided into 10 folds, and the model is trained 10 times, each time using a different fold as the testing set and the remaining folds as the training set. The resulting root mean square errors (RMSEs) are then averaged to obtain the final RMSE, providing a more reliable evaluation of the model's performance.

ANN Algorithm Development. To develop a multilayer perceptron (MLP) regression model for the new dataset, we implemented a Python-based ANN using the MLP Regressor from the Sci-kit learn library,[35] following the customized model development steps outlined in our previous work.[18] The model had an input layer with 15 features, 1 hidden layer, and an output layer with one unit. We trained the model with the newly cleaned training dataset and used the mean square error (MSE) as the loss function during training.[36]

https://doi.org/10.1021/acsomega.3c01676
ACS Omega 2023, 8, 17220−17233

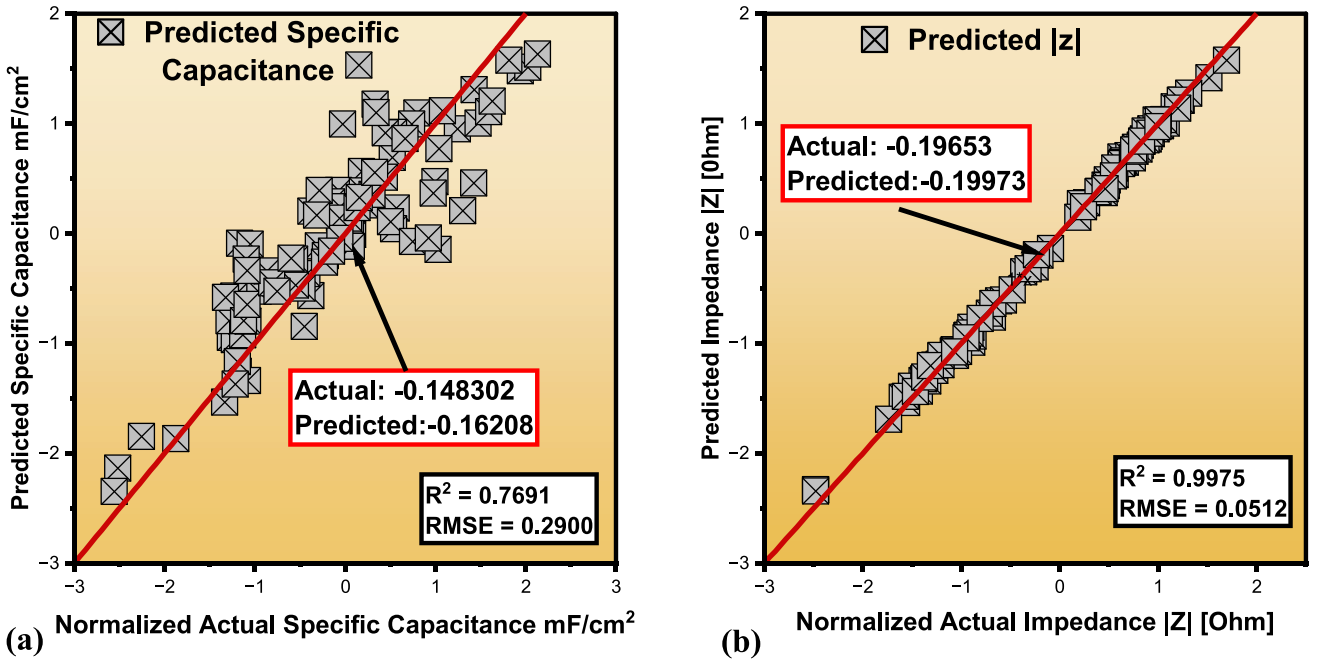

Figure 4. (a) Comparison is conducted between the specific areal capacitance values obtained experimentally and the predictions made using the test set with the multilayer perceptron (MLP) model. (b) Comparison is carried out between the magnitude of impedance (|Z|) obtained experimentally and the predictions made using the test set with the MLP model.[18] The purpose of showing the red boxes is to provide an example of how well the predictions made by a model match up with the actual values observed in the data.

$$\mathrm{MSE} = \frac{1}{K}\sum_{i=1}^{K}(y(i) - \hat{y}(i))^2 \tag{3}$$

The experimental values are represented as $y(i)$, the estimated values are represented as $\hat{y}(i)$, and K represents the number of data points.

To optimize the weights, we used the Adam optimization algorithm with a learning rate of 0.001 and a batch size of 16. The model was trained for 500 epochs. The activation function of the hidden layer output is given by[37]

$$v_j^l = f\left(\sum_{i=1}^{j-1}(w_{ji}^l \alpha_i)\right) \tag{4}$$

where l denotes the index of the hidden layer, j represents the number of neurons in the lth hidden layer $j \in Z^+$, $j-1$ denotes the number of neurons in the $(l-1)$th hidden layer, and α represents the number of features for the layers. We used the rectifier linear unit (ReLU) as the activation function, similar to our previous work.[18] However, we randomly initialized the weights (w_{ji}^l) between layers, which could result in differences in the model's performance. By making these changes, we ensured that the model was not the same as the one developed in our previous work while still maintaining the same evaluation metric.

To determine the optimal MLP design and hyperparameters for this new dataset, we employed a k-fold cross-validation (CV) approach with $k = 100$. The training data was split into 100 equally sized segments, and the root mean square error (RMSE) was calculated for each segment. The average of these RMSEs was taken as the RMSE for the set of hyperparameters of that network. The set of hyperparameters that yielded the lowest RMSE was selected as the optimal design for the network.[38]

Evaluation Metrics for ANN Algorithm Performance. Two key metrics are used to evaluate the performance of the model proposed in this study, namely, the root mean square error (RMSE) and the coefficient of determination (R^2).[39,40] RMSE is a widely used index that quantifies the discrepancy between the actual and predicted values of the response variable. It is calculated using the following equation:[40]

$$\mathrm{RMSE} = \sqrt{\frac{1}{K}\sum_{i=1}^{K}(y(i) - \hat{y}(i))^2} \tag{5}$$

where $y(i)$ represents the experimental value, $\hat{y}(i)$ is the estimated value, and K is the number of data points. The coefficient of determination (R^2) measures the degree of fit of a regression model to the data, with values ranging from 0 to 1.[36] A higher R^2 value indicates a better fit of the model to the data, with values close to 1 indicating a good fit and values close to 0 indicating a poor fit.[41] The formula for R^2 is as follows:[41,42]

$$R^2 = 1 - \frac{\sum_{i=1}^{K}(\hat{y}(i) - \overline{y}(i)}{\sum_{i=1}^{K} y(i) - \overline{y}(i)} \tag{6}$$

where $y(i)$ present the experimental value, $\hat{y}(i)$ is the estimated value, $\overline{y}(i)$ is the mean values of all the data points, and K is the number of data points. This formula for R^2 involves calculating the ratio of the explained variance to the total variance and subtracting the result from 1. The explained variance is the sum of the squared differences between the predicted values and the mean of the actual values, while the total variance is the sum of the squared differences between the actual values and their mean, across all data points.[42]

ELECTROCHEMICAL BEHAVIOR PREDICTION OF PSEUDOCAPACITOR ELECTRODES VIA THE ANN

Specific Capacitance and Impedance Prediction Based on the Test Dataset. The trained ANN model is tested for its ability to predict electrochemical behavior metrics by loading it with the test dataset. This dataset is divided into

https://doi.org/10.1021/acsomega.3c01676
ACS Omega 2023, 8, 17220−17233

80% training data and 20% test data. The results are presented in Figure 4, which displays parity plots of the test sets for the ANN model.[18] The MLP model shows an RMSE of 0.0512 in predicting impedance |Z|, as shown in Figure 4a. The accuracy of the developed ANN model is also evaluated by predicting the specific capacitance value using the test dataset. The MLP model has an RMSE of 0.2900 in this evaluation. The MLP model provides the best fit for predicting |Z|, as indicated by the R^2 value of 0.9959, as shown in Figure 4b.[18] Similarly, for the specific capacitance, the MLP model has the best fit with an R^2 value of 0.7691.[18]

Specific Capacitance and Impedance Prediction Based on Cross-Validation. Additionally, the regression accuracy of the MLP model is confirmed using cross-validation, which assesses the model's performance on a smaller data sample.[18] The RMSE scores of the ANN algorithm are shown in Table 2. The MLP approach proves to have the best accuracy,

Table 2. Performance Comparison of ML Algorithms Based on Cross-Validation

learning algorithms	MLP
performance metrics	RMSE
impedance |Z| [ohm]	0.0393
specific capacitance [mF/cm^2]	0.4401

with an RMSE score of 0.0393 in predicting the |Z| value. The RMSE score for forecasting specific capacitance is 0.4401, as determined in the earlier dataset splitting method.[18]

ANN-Enabled Optimization for Enhancing Electrochemical Behavior of Pseudocapacitors Electrode. One of the main goals of our research was to customize the ANN model that we had previously constructed, so that it could be used to predict the electrochemical behavior of pseudocapacitor electrodes and subsequently be used in an optimization problem.[18] Specifically, our optimized ANN model was designed to predict two important parameters: the impedance (|Z|) and specific capacitance of the pseudocapacitor. The results of our study showed that our customized ANN model was highly effective in accurately forecasting |Z| and specific capacitance, as evidenced by the low root mean square error (RMSE) values obtained. Another key objective of our study was to determine the optimal laser parameters for enhancing the electrochemical performance of pseudocapacitors. To achieve this, we used the trained ANN model as a black box to simulate the electrochemical behavior of pseudocapacitors based on different laser parameters. To find the optimal laser fabrication parameters, we used the SA optimization algorithm to maximize the objective function of the ANN model. Our goal was to identify the laser parameter settings that would yield the highest specific capacitance value. This approach holds significant promise for the design and optimization of pseudocapacitor electrodes with improved electrochemical performance. In this section, we first discuss the rationale behind using the SA algorithm and then explain how we formulate the optimization problem using SA.

Simulated Annealing. SA is a heuristic optimization algorithm that is based on the Monte Carlo search method and resembles the cooling process used for molten metals during annealing. SA typically starts with a random initialization, and the current state is then stochastically perturbed to reach a new state.[43,44] In the case of molten metals, the internal energy (E) tends to decrease spontaneously, but higher internal energy levels can also be accepted with a certain probability. For optimization purposes, the internal energy can be regarded as the fitness function, and the mechanism for accepting the new solution is based on the Metropolis algorithm. The Metropolis algorithm dictates that the probability of accepting a new solution is related to the annealing temperature, which is given by eq 7.[45] This equation shows that the probability of acceptance increases at higher temperatures, while at lower temperatures, the solution tends to remain unchanged.[45,46]

$$P_{ij} = \begin{cases} 1, E_j < E_i \\ \exp\left(-\frac{E_j - E_i}{T}\right), E_j \geq E_i \end{cases} \quad (7)$$

The probability of accepting the current solution (P_{ij}) is determined by the Metropolis algorithm, where "i" represents the previous iteration and "j" refers to the current iteration. The optimizing function is the internal energy (E), and the annealing temperature (T) determines the probability of accepting the new solution. The process involves several iterations to search for the optimal solution, and the temperature is gradually reduced at an extremely slow rate to ensure the precision of the solution. At the end of each iteration, annealing takes place, and the annealing temperature is reduced using eq 8[45,47]

$$T_{K+1} = T_K \times K \quad (8)$$

where K represents the annealing rate. This is because slower annealing tends to provide better precision. The global search for a feasible solution depends on the number of iterations, which can be increased by using a higher annealing temperature and a slower cooling scheme. This approach can lead to better performance by allowing the algorithm to explore a wider range of solutions. Additionally, the independent initialization of the algorithm allows for a more comprehensive search for the optimal solution.

Simulated Annealing Implementation for Laser Parameter Fabrication. The SA method is implemented based on the laser fabrication parameters and the trained MLP model. In algorithm 1, the first step is to call the trained MLP function using a vector x_n, which includes all eight laser fabrication parameters for asymmetric optimal design, and four laser fabrication parameters for symmetric optimal design. The SA algorithm recommends two sets of four laser parameters for asymmetric optimal design, which fabricate two different electrodes, and one set of laser fabrication parameters for symmetric optimal design, which fabricate both electrodes.

Various parameters need to be initialized, including the initial temperature, the lower temperature limit, cooling schedule rate, the number of iterations, the objective function, and the initial solution (see Table 3). The cooling schedule rate should be moderate, as a too high rate can cause the algorithm to converge to a local optimal solution, while a too slow rate can result in a longer search time.[48,49] After initializing the parameters, the initial solution is evaluated using the objective function, which

Table 3. SA Parameters for Optimal Electrode Design

parameters	description	value
T_{max}	initial temperature	1000
T_{min}	lower temperature limit	0.001
K	cooling schedule	0.9
$N_{iteration}$	iterations per temperature	1000

https://doi.org/10.1021/acsomega.3c01676
ACS Omega 2023, 8, 17220−17233

Table 4. SA Optimal Laser Fabrication Parameters for Electrode Design

	base electrode				changing electrode			
optimal Solutions	power (W)	frequency (kHz)	pulse duration (ns)	scan speed (mm/s)	power (W)	frequency (kHz)	pulse duration (ns)	scan speed (mm/s)
asymmetric (OPT-ASY)	13	100	2	5	17	600	1	290
symmetric (OPT-SYM)	20	600	1	10	20	600	1	10

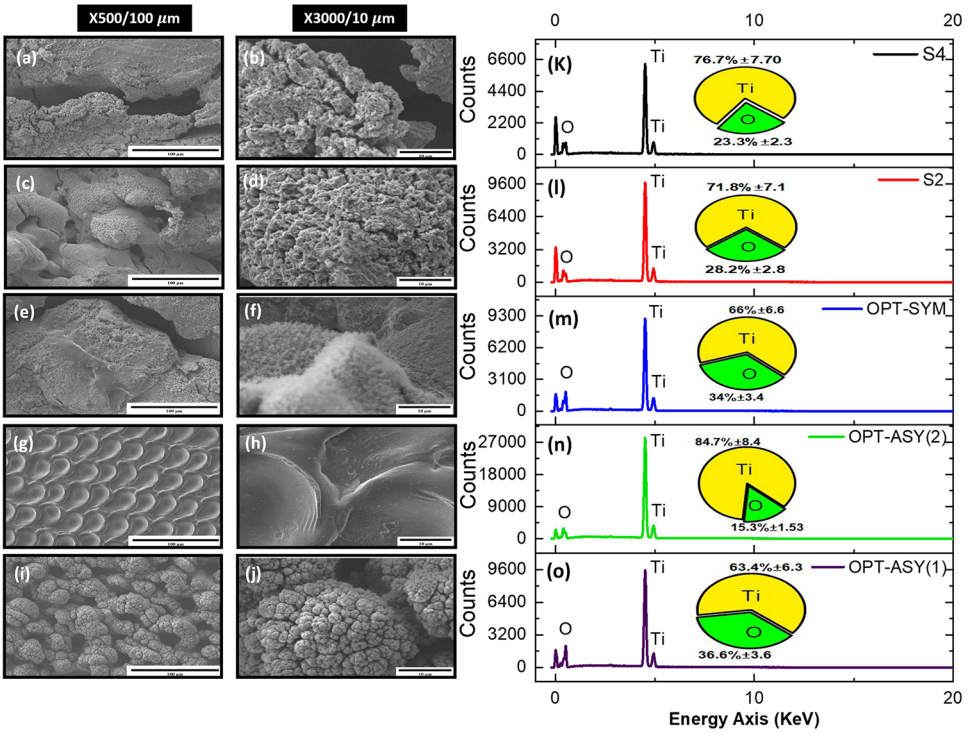

Figure 5. Morphological characterization was conducted using SEM images with EDX element mapping (weight %). The EDX data demonstrates elemental composition and the presence of oxygen caused during laser irradiation. The samples analyzed were the following: S4 at ×500 magnification (100 μm) and ×3000 magnification (10 μm) (a, b, respectively); S2 at ×500 magnification (100 μm) and ×3000 magnification (10 μm) (c, d, respectively); OPT-SYM at ×500 magnification (100 μm) and ×3000 magnification (10 μm) (e, f, respectively); OPT-ASY (2) at ×500 magnification (100 μm) and ×3000 magnification (10 μm) (g, h, respectively); OPT-ASY(1) at ×500 magnification (100 μm) and ×3000 magnification (10 μm) (i, j, respectively). The EDX results are presented in images (k−o). Images (b, d, f, h, j) were taken at ×3000 magnification (10 μm) to provide a closer view of the samples.

aims to maximize the specific areal capacitance ($\max f(x_n)$). The algorithm calculates the difference between the current solution value and the previous accepted solution value.[50] If this difference is less than zero, the solution corresponding to the current function value is updated to the solution after the loop is executed. On the other hand, if the difference is greater than or equal to zero, the solution corresponding to the current function value is updated to the solution after the loop with a certain probability.[50] This process will be repeated N times where N is the number of iterations in each temperature. The current temperature is updated using the cooling schedule rate after each cycle until the end of the cycle, and the optimal solution is obtained at the end of the cycle. Lastly, the SA algorithm recommended eight different laser fabrication parameters for asymmetric optimal design and four different laser fabrication parameters for symmetric optimal design, which can be found in Table 4.

Algorithm 1: SA for Optimal Electrode Design

1: $f(x_n)$; $x_n = \{x_1, x_2 x_3 x_4 x_5 x_6 x_7, x_8\}$ ▶ Call the MLP function based on the input laser parameters (power, frequency, pulse duration, and scan speed).

2: $T = T_{max}$; $K = 0.9$; $N = 1000$; ▶ set the initialization of all parameters, including temperature T, iteration N, cooling rate K.

3: $x_{current} = rand\ (x_n)$; ▶ Random initial solution.

4: $f(x_n) \rightarrow Specific\ areal\ capacitance\ f(x_n)$ ▶ The initial solution is evaluated using the objective function.

5: **While** $T > T_{max}$ ▶ Verify the temperature of the outer loop.

6: N = 1:1000 $x_{n,new} = Generator\ (x_n)$ ▶ Change one parameter in x_n in the constraint range (Range of parameters when have limits based on other parameters)

7: Evaluate: $f(x_{n,new})$ ▶ Calculate change of energy level. Integrating the solution for improvement.

if $f(x_{n,new}) > f(x_n)$ **accept**

else { **if** $e^{-\{f(x_n) - f(x_{n,new})\}} < rand\ (0,1)$ x_{rej} ▶ Acceptance with probability function.

end

$T = T * K$ ▶ Reduce the temperature

if $T < T_{min}$ ▶ End of optimization

end

RESULTS AND DISCUSSION

Morphology and Structural Properties of Electrodes.

Following the optimization of sample preparation, six samples

https://doi.org/10.1021/acsomega.3c01676
ACS Omega 2023, 8, 17220−17233

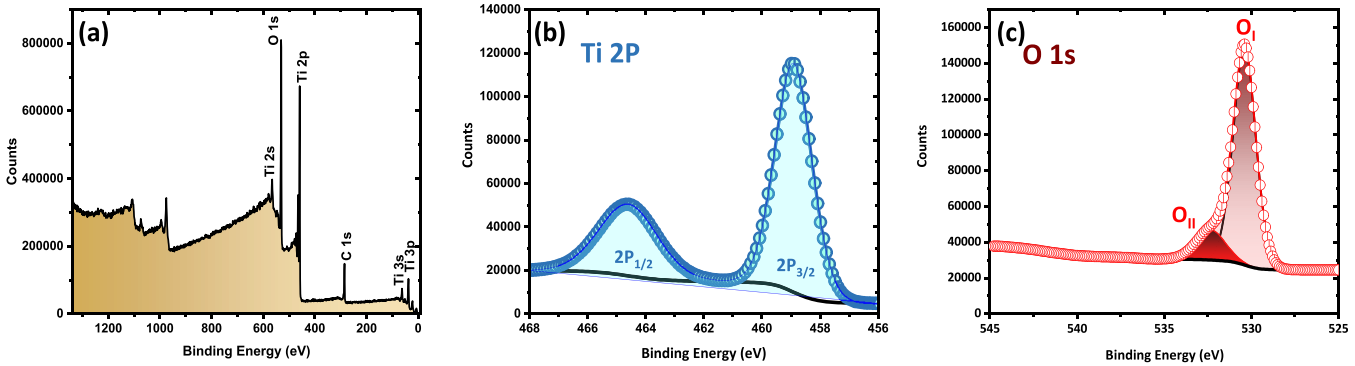

Figure 6. (a) Survey scan of the XPS spectrum demonstrates Ti and O species. (b) Ti 2p peak. (c) O 1s core levels with deconvoluted two peaks.

were selected for analysis of structural and morphological changes. Laser-induced porous structures offer increased surface area and porosity, which enhances the electrode's capacitance behavior by enabling more ions to adsorb during charge and discharge processes.[18] Additionally, increased oxidized surface area offers more available redox-active sites. We compared the non-optimized and optimized sample sets to illustrate these changes more clearly. In the non-optimized sample group, S2 and S4 were selected, where the laser parameters remained constant with power set to 10 W, frequency set to 900 kHz, and pulse duration of 0.15 ns, while the scan speed was set at 10 mm s^{-1}. For S4, all the parameters remained the same as S2, except the frequency was increased to 1200 kHz. In the optimized samples we selected OPT-SYM and OPT-ASY (see Table 4). Results indicate that laser ablation parameters significantly impact the surface morphology of treated samples. Figure 2 depicts SEM images and EDX results showing that surface properties of ablated samples vary depending on the laser parameters used.

All samples were SEM imaged at ×500 (100 μm) and ×3,000 (10 μm) magnifications, as shown in Figure 5. The OPT-SYM and OPT-ASY electrodes differ significantly. Electrodes S2 and S4 exhibit very small changes to the pretreatment Ti surface, whereas sample S2 has a slightly better surface but lacks the necessary porous structure to enhance surface area (see Figure 5a−d). The discrepancies in the distribution of the porous structure between S2 and S4 show that there may be an optimal frequency for generating a more equally distributed porous structure. The EDX data indicates that at a lower frequency of 900 kHz, there is a higher oxidation percentage of 28.2% and lower Ti percentage of 71.8%. This can be attributed to the fact that with each pulse, the maximum surface temperature of the irradiation zone increases, leading to higher energy. However, when the frequency is increased to 1200 kHz, the oxidation percentage drops to 23.3%, and the Ti percentage increases. This suggests that there might be a threshold frequency beyond which any further increase in frequency would not have a significant impact on oxidation and surface morphology.

In contrast, the optimized samples exhibit distinct differences in surface morphology. OPT-ASY (1) employed a slower scan speed and lower frequency, which resulted in greater energy transfer or induction onto the surface of the Ti substrate, leading to the growth of a self-standing 3D nanostructured oxide layer and extensive surface oxidation. OPT-ASY (1) displays a macroporous structure resembling broccoli and a white and black oxide layer, indicating an increase in surface area and redox active sites (see Figure 5i,j). On the other hand, OPT-ASY (2) utilized a higher scan speed (290 mm s^{-1}) and frequency with lower pulse duration, which produced a uniformly distributed structure with visible holes and grooves without any 3D nanostructured oxide layer (see Figure 5g,h). By increasing the power to 20 W in OPT-SYM with a scan speed of 10 (mm s^{-1}), a spongy porous microstructure was obtained, resulting in a successful phase change as more energy or power was transferred or induced onto the surface of the Ti substrate (refer to Figure 5e). At ×3,000 magnification, the SEM image of OPT-SYM depicts millions of microgranules that have grown and agglomerated on top of the standing structures, resembling the top view of a broccoli (refer to Figure 5f). The formation of standing structures is consistent throughout the entire surface, and the differences observed in surface morphology can be attributed to the amount of time allotted for the laser beam to traverse and ablate the surface. These differences are evident in the EDX results, which show variations in the degree of oxidation that occurred during the laser irradiation process.[18] Slower scan speeds used in OPT-ASY (1) and OPT-SYM allow for more interaction time between the laser and the titanium substrate, resulting in higher oxidation levels and a higher percentage of oxygen detected in the EDX map spectrum. Conversely, higher scan speeds in OPT-ASY (2) result in lower oxidation levels and a higher percentage of titanium detected. Despite the increase in frequency, the morphology still exhibits a fibrous and porous microstructure, indicating the significance of power and scan speed. The study of how the power level and scan speed of the laser impact the surface properties of the Ti substrate is intriguing, especially with regard to the degree of oxidation and the resulting microstructure. It appears that a higher power level and lower scan speed result in increased energy transfer to the surface, leading to a more significant phase change and increased oxidation traces, resulting in a more porous microstructure. This is desirable for increasing surface area and improving capacitance behavior.

XPS was conducted on all the samples to analyze the surface chemical bonding and cation oxidation states of the laser-assisted fabrication. The XPS survey spectrum for one of the samples (Figure 6a) confirms that the film mainly consists of titanium and oxygen, with some additional carbon. A similar composition is observed in the survey spectra for the OPT-ASY (1) sample. The high-resolution XPS spectrum of the Ti 2p region shown in Figure 6b is deconvoluted into two peaks, Ti $2p_{3/2}$ and Ti $2p_{1/2}$, which are located at 458.91 and 464.58 eV, respectively.[51,52] This is a typical signature for stoichiometric TiO. The O 1s core-level spectra for OPT-ASY (1) are shown in Figure 6c, and the decomposition is performed using two contributions denoted as O_I (530.38 eV) and OII (531.84 eV).[53] The low-energy peak O_I is assigned to the Ti−O bond,

https://doi.org/10.1021/acsomega.3c01676
ACS Omega 2023, 8, 17220−17233

while the peak at higher binding energies, O_{II}, corresponds to C−O bonds.[53]

X-ray diffraction (XRD) analysis was employed to confirm the presence of micro- and nanoweb-like structures of titanium oxide in one electrode. The XRD patterns revealed the formation of a crystalline structure consisting of rutile and anatase phases, as shown in Figure 7. The dominant phase was found to be rutile, as evidenced by the major peaks observed at 26.8°, 35.6°, 40.5°, 53.6°, 63.4°, 68.6°, and 69.4°, which correspond to (1 1 0), (1 0 1), (1 1 1), (2 1 1), (3 1 0), (3 0 1), and (1 1 2), respectively (according to JCPDS card No. 88−1175).[54,55] The anatase phase was also present, with peaks observed at 38.4°, 55.9°, and 62.3° corresponding to (0 0 4), (2 0 0), and (2 0 4), respectively (according to JCPDS card No. 21−1272).[15,55,56] The anatase phase is known for its higher surface area and narrow band, which make it more suitable for energy conversion applications. However, it is also known to have more surface defects. On the other hand, the rutile phase is generally known for its tetragonal crystal structure, higher density, and thermal stability, making it more durable and suitable for higher power applications. The presence of a mixed state allows for a combination of both phases on the surface, which may provide a desirable combination of properties for various applications.

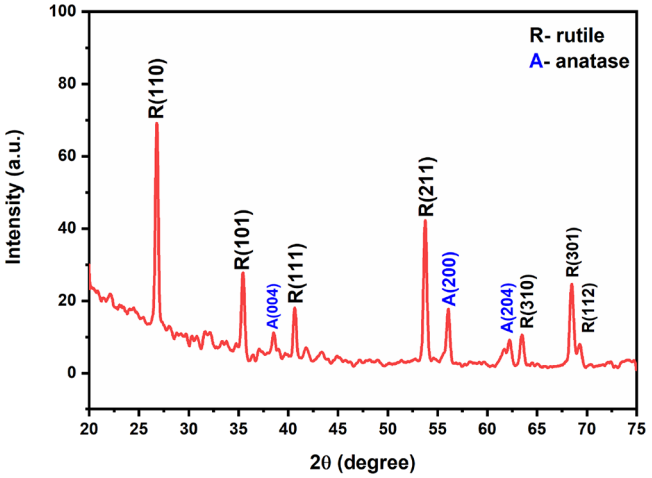

Figure 7. XRD analysis of electrode fabricated using the ULPING technique.

Electrochemical Properties of Electrodes. The purpose of the electrochemical analysis was to confirm the results obtained from the microscopy and characterization analysis with respect to the effect of laser parameters on surface characterization improvement.[18] The electrochemical analysis included CV, GCD, and EIS to determine whether the observed structural modifications had an impact on the electrochemical properties of the samples. The results of the electrochemical analysis were then compared to the findings from the microscopy and characterization analysis to establish a correlation between the two. This allowed for a more complete understanding of the impact of the laser parameters on both the physical and electrochemical properties of the samples.

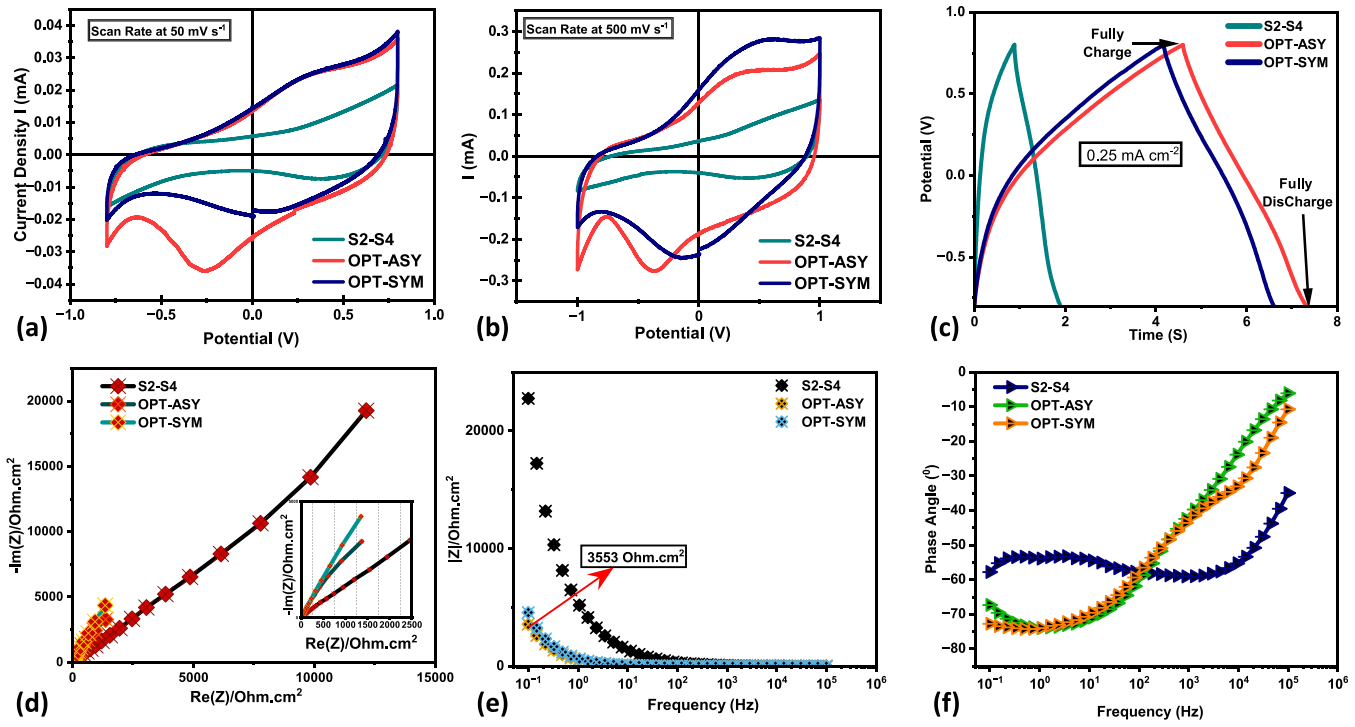

Figure 8. (a) CV profile of all samples at 50 mV s^{-1} scan speed. (b) CV curve of all samples at 500 mV s^{-1} scan rates. (c) GCD curves were generated at a constant current density of 0.25 mA cm^{-2}, OPT-ASY exhibits a larger charge depletion compared to OPT-SYM and S2−S4. (d) Nyquist impedance analysis of all the samples. (e) OPT-ASY demonstrates the least impedance. (f) Bode plot of samples to achieve a near 80° phase angle for capacitive characteristics. These results suggest that OPT-ASY is the most promising sample with superior electrochemical behavior, demonstrated by its lower impedance and larger charge depletion in GCD. The CV and GCD curves also indicate that samples with increased surface area perform better. The Nyquist and Bode plots further support this observation, with OPT-ASY showing the least impedance and closest phase angle to the ideal capacitance phase angle. Overall, these findings suggest that optimizing surface area can lead to improved electrochemical performance in the tested samples.

https://doi.org/10.1021/acsomega.3c01676
ACS Omega 2023, 8, 17220−17233

The electrode's electrochemical redox and capacitive behavior was analyzed using a CV curve. As shown in Figure 8a,b, the CV curve indicates a typical Faradaic dominant reaction. Figure 8a,b illustrates the CV curves of the chosen electrodes in a 1 M sodium sulfate (Na_2SO_4) electrolyte, with a potential range of −0.8 to 0.8 V and scan rate of 50 mVs^{-1}, as well as a potential range of −1 to 1 V with a scan rate of 500 mVs^{-1}. The electrolyte composition, which remained consistent across all setups, may affect the electrochemical performance of the samples, although it was not considered in this study.[18] The redox peaks exhibited excellent reversibility and rapid kinetics occurring at the oxide surface, while the capacitive nature of the samples was evident in the −0.8 to 0.8 V range. The samples' rapid, reversible redox behavior and capacitive characteristics confirm the presence of pseudocapacitance, thereby confirming the device as a pseudocapacitor from a scientific perspective.

Among the analyzed samples, OPT-ASY demonstrated the best capacitive performance. S2−S4, on the other hand, showed the lowest current density of 0.021 mA at 0.8 V due to their low oxidation and surface area. OPT-SYM's current density at 0.8 V (0.038 mA) improved slightly due to its increased surface area and oxidation rate. At a scan rate of 500 mV s^{-1}, OPT-SYM exhibits a symmetric CV shape, further confirming that the symmetric fabrication parameters recommended by the optimization algorithm result in excellent performance. The supercapacitive performance of OPT-ASY, which is a combination of different laser parameters, was found to be significantly better than those of other samples in all groups, as indicated by its CV curve that had a nearly rectangular shape and the highest rechargeable current density. This superior performance was attributed to the faster oxidizing rate and the presence of 3D nanoporous structures, which were responsible for creating the best electrode behavior among all samples according to the CV results. Both SEM images and EDX data indicate that the surface area and oxidation rate were important factors in the electrochemical behavior of OPT-ASY. Furthermore, the enhanced pattern generated by adjusting the laser parameters was noticeable in the CV curves of all other sample groups as well.

A GCD test was used to evaluate the capacitive charge of the fabricated samples. The test involved analyzing the discharge and charge curves for all cell setups using a constant current density of 0.25 mA cm^{-2} within the stable potential range of −0.8 to 0.8 V. As shown in Figure 8c, the GCD plot of all sample groups confirmed the improvement pattern resulting from changing the laser parameters, consistent with the CV and microscopy results. OPT-ASY exhibited the best performance, not only within the optimized samples but also across other sample groups, depleting stored charges in 3.1498 s. In comparison, OPT-SYM and S2−S4 depleted charges in 2.9091 and 1.015 s, respectively. OPT-ASY and OPT-SYM's exceptional performance was mainly attributed to the reduction in the redox event that caused charge depletion as well as the improved specific surface area. Once again, the microscopy analysis revealed an improvement pattern from non-optimized samples to optimized samples, demonstrating the crucial role of improved surface morphology in enhancing the electrochemical behavior of the samples.

EIS is commonly used along with CV, and it relies on a continuous DC bias and a low amplitude alternating current (AC) signal.[18] To study the samples, EIS measurements were conducted on all groups, covering a frequency range of 100 mHz to 100 kHz.[18] The Nyquist and Bode graphs of the samples are depicted in Figure 8d−f. The EIS measurements also demonstrated a noticeable pattern of improvement, reinforcing the correlation between increased electrode surface area and improved electrochemical performance. This pattern of improvement was apparent in Figure 7d, which represents the impedance data for each sample as a sum of their real and imaginary components. The summation of real and imaginary components varied across the samples, ranging from as high as 20,000 Ω cm^2 in S2−S4 to as low as 3500 Ω cm^2 in OPT-ASY. EIS measurements can provide information about electrode conductivity, which is a critical parameter. Figure 8e displays the electrode impedance plotted against frequency for each sample group. Out of all the samples tested, OPT-ASY, which had the most favorable surface area for interfacial charge storage, exhibited the lowest electrode resistivity (3554 Ω cm^2). The electrodes with the highest performance in microscopy, CV, and GCD, including the optimized ones, also showed lower electrode resistivity. The Bode plot, as shown in Figure 8f, was utilized to investigate the capacitance behavior and diffusion properties of the electrodes. The Bode figure typically shows the phase angle vs frequency, with −90° being the ideal capacitance phase angle.[18] Both the Nyquist and Bode analyses indicate a consistent trend, whereby electrodes displaying superior performance within each group demonstrate lower impedance and a phase angle approaching −90° at lower frequencies. For instance, within the optimized group, the phase angle of OPT-ASY is in very close proximity to −70°, the OPT-SYM value is close to −75°, and in the non-optimized electrode group, S2−S4 values also approach −60°. The results of the study suggest that samples with larger surface areas display improved charge transfer, superior electrochemical performance (characterized by lower impedance), and phase angle values that approach the ideal capacitance phase angle. It should be noted that the electrolyte utilized in this investigation was a basic salt solution, which exhibits lower conductivity in comparison to highly acidic or basic aqueous solutions.

As previously stated, it is possible to compute the particular areal capacitance of each sample by utilizing eq 1 and analyzing the GCD curve.[18] In order to assess the functional capability of the constructed electrodes, it is essential to calculate two key parameters, namely, energy density (E_S) and power density (P_S), which can be determined by utilizing eqs 9 and 10, respectively, and utilizing the specific areal capacitance obtained from the analysis.[29,57,58]

$$E_S = \frac{1}{2C_A \Delta V^2} \tag{9}$$

$$P_S = 3600E_S/\Delta t \tag{10}$$

where C_A is the specific areal capacitance computed from GCD, $\Delta V$is the potential window, and Δt is the discharge time. It is worth noting that a remarkable specific areal capacitance of 0.9999 mF/cm^2 was attained at a current density of 0.25 mA/cm^2, resulting in a maximum energy density and power density output of 0.001279872 Wh/cm^2 and 1.46283734 W/cm^2, respectively. To conduct further morphological analysis, the ImageJ software was employed to determine the topological characteristics of the ablated surface through the examination of SEM images following our previous work.[18] Table 5 presents the specific areal capacitance, energy density, power density, and porosity measurements of all samples. Remarkably, a tendency toward improvement can also be shown; the particular areal

https://doi.org/10.1021/acsomega.3c01676
ACS Omega 2023, 8, 17220−17233

Table 5. Summary of the Specific Areal Capacitance, Porosity, Energy Density, and Power Density of the Selected Samples

sample	specific areal capacitance (mF/cm^2) @ current density (0.25 mA/cm^2)	porosity (%)	energy density (Wh/cm^2)	power density (W/cm^2)
OPT-ASY	0.9999	42.35	0.001279872	1.46283734
OPT-SYM	0.8575	33.35	0.0010976	1.3217019
S2-S4	0.3579	23.8/22.6	0.000458112	1.623886805

capacitance and porosity increased together with the sample surface area.

DISCUSSION

As we showed in this study, the morphology, nanofiber generation, and porosity of pseudocapacitor electrodes are primarily determined by the parameters of an ultrashort pulse laser. The theory behind the nanofiber generation is straightforward and simple: when the laser pulses irradiate the substrate surface, a considerable amount of energy is transferred, converting photon energy into heat energy. Several events occur during this brief period to facilitate successful growth of nanostructure on the surface. Subsequently, a plasma plume is formed, causing ionization, which enables the laser-affected zone to interact with the ambient atmosphere and oxygen to create an oxidized surface. The morphology and presence of nanostructure are influenced by the pulse energy and peak pulse power utilized, which are directly related to the heat affected zone (HAZ) and temperature gradient. The aim is to use an efficient and effective pulse energy and peak power to avoid thermal and mechanical damage, minimize particle agglomeration, and prevent the evaporation or sublimation of the nanostructure. Following the ionization process, the laser-irradiated local spot cools and crystallizes, resulting in a sufficiently oxidized surface and nanostructure, provided that the appropriate parameters are used. Our study demonstrates that the use of SA as an optimization algorithm can provide valuable insights into the impact of laser parameters on the electrochemical performance of electrodes. SA enabled a more comprehensive exploration of laser parameter space, including previously inaccessible parameter combinations, and identified optimal electrode fabrication conditions that would have been challenging to find using non-optimized methods. For instance, we found that low scan speeds and frequencies, a moderate power range, and a pulse duration of 2 (ns) in OPT-ASY resulted in superior electrochemical performance. Our results indicate that optimization algorithms like SA have significant potential in electrode design tasks not only for supercapacitors but also for other types of electrochemical energy storage devices. Optimization can efficiently identify optimal parameter settings that are difficult or time-consuming to obtain through trial-and-error experimentation. Thus, optimization algorithms can lead to the development of novel and improved electrode designs that enhance the performance and efficiency of energy storage devices, thereby advancing energy storage technologies.

CONCLUSIONS

In this study, our first aim was to establish the relationship between the laser parameters used in the fabrication of pseudocapacitor electrodes and their electrochemical performance through data-driven ML approaches. Subsequently, we investigated how an optimization algorithm, simulated annealing, could be used to find the most optimal laser parameters for achieving the most efficient electrochemical performance of the fabricated electrodes. To accomplish this, we generated a large dataset that included laser parameters selected experimentally and electrochemical behavior performance metrics obtained from different microscopy and electrochemistry analyses. We then used a customized ANN model to highlight the relationship between laser parameters and electrochemical performance metrics such as specific areal capacitance and impedance. Finally, we employed an SA optimization algorithm to maximize the objective function, which, in our case, was the specific capacitance value and determine the most optimal laser fabrication parameters. Our results showed that the specific areal capacitance increased from 0.3579 mF cm^{-2} in non-optimized electrodes to 0.9999 mF cm^{-2} at a current density of 0.25 mA cm^{-2} in optimized electrodes. The use of SA improved the pseudocapacitor performance and can be employed in optimal design procedures.

ASSOCIATED CONTENT

Data Availability Statement

The corresponding author of this paper will provide the original data upon request. All the original code that was generated as part of this study will be shared by the corresponding author upon request.

AUTHOR INFORMATION

Corresponding Author

Amirkianoosh Kiani − *Department of Mechanical and Manufacturing Engineering, Ontario Tech University, Oshawa, Ontario L1G 0C5, Canada; Silicon Hall: Micro/Nano Manufacturing Facility, Faculty of Engineering and Applied Science, Ontario Tech University, Oshawa, Ontario L1G 0C5, Canada;* orcid.org/0000-0002-9125-3219; Email: amirkianoosh.kiani@ontariotechu.ca

Author

Kavian Khosravinia − *Department of Mechanical and Manufacturing Engineering, Ontario Tech University, Oshawa, Ontario L1G 0C5, Canada; Silicon Hall: Micro/Nano Manufacturing Facility, Faculty of Engineering and Applied Science, Ontario Tech University, Oshawa, Ontario L1G 0C5, Canada;* orcid.org/0000-0002-8069-4596

Complete contact information is available at: https://pubs.acs.org/10.1021/acsomega.3c01676

Author Contributions

K.K.: methodology, visualization, investigation, software, data collection and data analysis, writing − original draft preparation. A.K.: conceptualization, supervision, methodology, investigation, validation, data curation, writing − reviewing and editing.

Notes

The authors declare no competing financial interest.

ACKNOWLEDGMENTS

This research is partially funded by the Natural Sciences and Engineering Research Council of Canada (NSERC).

REFERENCES

(1) Patel, M. R.; Beik, O. Wind and Solar Power Systems : Design, Analysis, and Operation. *Wind Solar Power Syst.* **2021**. DOI: 10.1201/9781003042952.

(2) Khot, M.; Kiani, A. A Review on the Advances in Electrochemical Capacitive Charge Storage in Transition Metal Oxide Electrodes for Pseudocapacitors. *Int. J. Energy Res.* **2022**, 21757.

(3) Mitali, J.; Dhinakaran, S.; Mohamad, A. A. Energy Storage Systems: A Review. *Energy Storage and Saving* **2022**, *1*, 166−216.

(4) Rehman, J.; Eid, K.; Ali, R.; Fan, X.; Murtaza, G.; Faizan, M.; Laref, A.; Zheng, W.; Varma, R. S. Engineering of Transition Metal Sulfide Nanostructures as Efficient Electrodes for High-Performance Supercapacitors. *ACS Appl Energy Mater* **2022**, *5*, 6481−6498.

(5) Orlando, J. D.; Lima, R. M. A. P.; Li, L.; Sydlik, S. A.; de Oliveira, H. P. Electrochemical Performance of N-Doped Carbon-Based Electrodes for Supercapacitors. *ACS Appl. Electron. Mater.* **2022**, *4*, 5040−5054.

(6) Pathak, M.; Rout, C. S. Hierarchical NiCo2S4 Nanostructures Anchored on Nanocarbons and Ti3C2Tx MXene for High-Performance Flexible Solid-State Asymmetric Supercapacitors. *Adv Compos Hybrid Mater* **2022**, *5*, 1404−1422.

(7) González, A.; Goikolea, E.; Barrena, J. A.; Mysyk, R. Review on Supercapacitors: Technologies and Materials. *Renewable and Sustainable Energy Reviews* **2016**, *58*, 1189−1206.

(8) Poonam; Sharma, K.; Arora, A.; Tripathi, S. K. Review of Supercapacitors: Materials and Devices. *J. Energy Storage* **2019**, *21*, 801−825.

(9) Fleischmann, S.; Mitchell, J. B.; Wang, R.; Zhan, C.; Jiang, D. E.; Presser, V.; Augustyn, V. Pseudocapacitance: From Fundamental Understanding to High Power Energy Storage Materials. *Chem. Rev.* **2020**, *120*, 6738−6782.

(10) Jiang, Y.; Liu, J. Definitions of Pseudocapacitive Materials: A Brief Review. *Energy Environ. Mater.* **2019**, *2*, 30−37.

(11) Simon, P.; Brousse, T.; Favier, F. Supercapacitors Based on Carbon or Pseudocapacitive Materials. 2017, 39−55, DOI: 10.1002/9781119007333.CH3.

(12) Mishra, N. K.; Mondal, R.; Maiyalagan, T.; Singh, P. Synthesis, Characterizations, and Electrochemical Performances of Highly Porous, Anhydrous $Co_{0.5}Ni_{0.5}C_2O_4$for Pseudocapacitive Energy Storage Applications. *ACS Omega* **2022**, *7*, 1975−1987.

(13) Wang, C.; Yan, B.; Zheng, J.; Feng, L.; Chen, Z.; Zhang, Q.; Liao, T.; Chen, J.; Jiang, S.; Du, C.; He, S. Recent Progress in Template-Assisted Synthesis of Porous Carbons for Supercapacitors. *Advanced Powder Materials* **2022**, *1*, 100018.

(14) Yin, J.; Zhang, W.; Alhebshi, N. A.; Salah, N.; Alshareef, H. N. Synthesis Strategies of Porous Carbon for Supercapacitor Applications. *Small Methods* **2020**, *4*, 1900853.

(15) Gholami, A.; Kiani, A. Laser-Induced Nanofibrous Titania Film Electrode: A New Approach for Energy Storage Materials. *J. Energy Storage* **2020**, *31*, No. 101654.

(16) Gholami, A.; Yim, C.-H.; Kiani, A.; Electrochemical, A.; Rahmani, M.; Ying, C.; Xu, L. Electrochemical Performance of Titania 3D Nanonetwork Electrodes Induced by Pulse Ionization at Varied Pulse Repetitions. *Nanomaterials* **2021**, *11*, 1062.

(17) Khot, M.; Kiani, A. Synthesis of Self-Grown Nanostructured NiO via Pulse Ionization for Binderless Psuedocapacitor Electrode. *J. Energy Storage* **2022**, *55*, No. 105779.

(18) Khosravinia, K.; Kiani, A. Unlocking Pseudocapacitors Prolonged Electrode Fabrication via Ultra-Short Laser Pulses and Machine Learning. *iScience* **2023**, *26*, No. 106438.

(19) Moghareh Abed, M.; Kiani, A. Optical Reflectivity of Heat-Treated Nanofibrous Silicon Thin-Films Induced by High Energy Picosecond Laser Pulses. *Sens Biosensing Res* **2020**, *30*, No. 100385.

(20) Li, Z.; Wei, X.; Yang, Z. Pulsed Laser 3D-Micro/Nanostructuring of Materials for Electrochemical Energy Storage and Conversion. *Prog. Mater. Sci.* **2023**, *133*, No. 101052.

(21) Yi, C. Q.; Zou, J. P.; Yang, H. Z.; Leng, X. Recent Advances in Pseudocapacitor Electrode Materials: Transition Metal Oxides and Nitrides. *Trans. Nonferrous Met. Soc. China* **2018**, *28*, 1980−2001.

(22) Kumar, A.; Rathore, H. K.; Sarkar, D.; Shukla, A. Nano-architectured Transition Metal Oxides and Their Composites for Supercapacitors. *Electrochem. Sci. Adv.* **2022**, *2*, No. e2100187.

(23) Singh, A. K.; Jaiswal, P.; Singh, P. A Review on Transition-Metal Oxalate Based Electrode for Supercapacitors. *IOP Conf. Ser. Mater. Sci. Eng.* **2021**, *1166*, No. 012032.

(24) Schneider, C. A.; Rasband, W. S.; Eliceiri, K. W. NIH Image to ImageJ: 25 Years of Image Analysis. *Nat. Methods* **2012**, *9*, 671−675.

(25) Zhu, S.; Li, J.; Ma, L.; He, C.; Liu, E.; He, F.; Shi, C.; Zhao, N. Artificial Neural Network Enabled Capacitance Prediction for Carbon-Based Supercapacitors. *Mater. Lett.* **2018**, *233*, 294−297.

(26) Wang, J.; Li, Z.; Yan, S.; Yu, X.; Ma, Y.; Ma, L. Modifying the Microstructure of Algae-Based Active Carbon and Modelling Supercapacitors Using Artificial Neural Networks. *RSC Adv.* **2019**, *9*, 14797−14808.

(27) Zhang, T.-B.; Liang, H.-J.; Rav, A.; Joshi, K. D.; Roy, K.; Ishtiyaq Ahmed, S.; Radhakrishnan, S.; Nair, B. B.; Thiruvengadathan, R. Efficient Hyperparameter-Tuned Machine Learning Approach for Estimation of Supercapacitor Performance Attributes. *J. Phys. Commun.* **2021**, *5*, 115011.

(28) Jha, S.; Bandyopadhyay, S.; Mehta, S.; Yen, M.; Chagouri, T.; Palmer, E.; Liang, H. Data-Driven Predictive Electrochemical Behavior of Lignin-Based Supercapacitors via Machine Learning. *Energy Fuels* **2022**, *36*, 1052−1062.

(29) Iqbal, M. Z.; Faisal, M. M.; Ali, S. R. Integration of Supercapacitors and Batteries towards High-Performance Hybrid Energy Storage Devices. *Int. J. Energy Res.* **2021**, *45*, 1449−1479.

(30) Miao, J.; Niu, L. A Survey on Feature Selection. *Proc. Comput. Sci.* **2016**, *91*, 919−926.

(31) Masoudi-Sobhanzadeh, Y.; Motieghader, H.; Masoudi-Nejad, A. FeatureSelect: A Software for Feature Selection Based on Machine Learning Approaches. *BMC Bioinformatics* **2019**, *20*, 1−17.

(32) Wilcox, R. R. *Introduction to Robust Estimation and Hypothesis Testing*; Elsevier, 2021. DOI: 10.1016/C2019-0-01225-3.

(33) Kumar, A.; Boehm, M.; Yang, J. Data Management in Machine Learning: Challenges, Techniques, and Systems. *Proceedings of the ACM SIGMOD International Conference on Management of Data* **2017**, *Part F127746*, 1717−1722.

(34) Sola, J.; Sevilla, J. Importance of Input Data Normalization for the Application of Neural Networks to Complex Industrial Problems. *IEEE Trans. Nucl. Sci.* **1997**, *44*, 1464−1468.

(35) Géron, A. *Hands-On Machine Learning with Scikit-Learn, Keras, and TensorFlow SECOND EDITION Concepts, Tools, and Techniques to Build Intelligent Systems;* O'Reilly Media, Inc., 2022.

(36) Frost, J. *Regression Analysis : An Intuitive Guide for Using and Interpreting Linear Models*; Statistics By Jim Publishing, 2020.

(37) Witten, H. I.; Frank, E.; Hall, A. H.; Pal, J. C. *Data Mining: Practical Machine Learning and Techniques*; Todd Green-Elsevier, 2017.

(38) Hussein, M. M.; Mutlag, H.; Shareef, H.; Wang, G.-J.; Li, S.-Y.; Qing, J.; Farizawani, A. G.; Puteh, M.; Marina, Y.; Rivaie, A. A Review of Artificial Neural Network Learning Rule Based on Multiple Variant of Conjugate Gradient Approaches. *J Phys Conf. Ser.* **2020**, *1529*, No. 022040.

(39) Wright, S. *Correlation and Causation*; USDA publications. 1921.

(40) Hodson, T. O. Root-Mean-Square Error (RMSE) or Mean Absolute Error (MAE): When to Use Them or Not. *Geosci. Model Dev.* **2022**, *15*, 5481−5487.

(41) Hahn, G. J. The Coefficient of Determination Exposed! *Chemtech.* **1973**, *3*, 609−612.

(42) Quinino, R. C.; Reis, E. A.; Bessegato, L. F. Using the Coefficient of Determination R2 to Test the Significance of Multiple Linear Regression. *Teach. Stat.* **2013**, *35*, 84−88.

(43) Rutenbar, R. A. Simulated Annealing Algorithms: An Overview. *IEEE Circuits Devices Mag.* **1989**, *5*, 19−26.

(44) Kirkpatrick, S.; Gelatt, C. D.; Vecchi, M. P. Optimization by Simulated Annealing. *Science* **1983**, *220*, 671−680.

(45) Zhou, S.; Liu, X.; Hua, Y.; Zhou, X.; Yang, S. Adaptive Model Parameter Identification for Lithium-Ion Batteries Based on Improved

https://doi.org/10.1021/acsomega.3c01676
ACS Omega 2023, 8, 17220−17233

Coupling Hybrid Adaptive Particle Swarm Optimization- Simulated Annealing Method. *J. Power Sources* **2021**, *482*, No. 228951.
(46) Najafabadi, H. R.; Goto, T. G.; Martins, T. C.; Barari, A.; Tsuzuki, M. S. G. Multi-Objective Topology Optimization Using Simulated Annealing Method. *Adv. Intell. Syst. Comput.* **2021**, *1296*, 343−353.
(47) Goto, T. G.; Najafabadi, H. R.; Duran, G. C.; Ueda, E. K.; Sato, A. K.; Martins, T. C.; Takimoto, R. Y.; Gohari, H.; Barari, A.; Tsuzuki, M. S. G.; Goto, T. G.; Najafabadi, H. R.; Duran, G. C.; Ueda, E. K.; Sato, A. K.; Martins, T. C.; Takimoto, R. Y.; Gohari, H.; Barari, A.; Tsuzuki, M. S. G. Versatility of Simulated Annealing with Crystallization Heuristic: Its Application to a Great Assortment of Problems. *Engineering Problems - Uncertainties, Constraints and Optimization Techniques*; IntechOpen 2021. DOI: 10.5772/INTECHOPEN.98562.
(48) Najafabadi, H. R.; Goto, T. G.; Falheiro, M. S.; Martins, T. C.; Barari, A.; Tsuzuki, M. S. G. Smart Topology Optimization Using Adaptive Neighborhood Simulated Annealing. *Appl. Sci.* **2021**, *11*, 5257.
(49) Najafabadi, H. R.; Goto, T. G.; Martins, T. C.; Barari, A.; Tsuzuki, M. d. S. G. Topology Optimization of Capacitive MEMS Accelerometers for Seismic Applications. *Lecture Notes on Data Engineering and Communications Technologies* **2023**, *146*, 760−772.
(50) Li, J.; Wang, Z.; Ma, S. Estimation of Health Status of Lithium-Ion Battery Based on PF-SA. *J. Phys. Conf. Ser.* **2021**, *2079*, No. 012008.
(51) Biesinger, M. C.; Payne, B. P.; Hart, B. R.; Grosvenor, A. P.; Stewart McIntryre, N.; Lau, L. W.; StC Smart, R. Quantitative Chemical State XPS Analysis of First Row Transition Metals, Oxides and Hydroxides; *Journal of Physics: Conference Series*; IOP Publishing 2008 DOI: 10.1088/1742-6596/100/1/012025.
(52) Biesinger, M. C.; Lau, L. W. M.; Gerson, A. R.; Smart, R. S. C. Resolving Surface Chemical States in XPS Analysis of First Row Transition Metals, Oxides and Hydroxides: Sc, Ti, V, Cu and Zn. *Appl. Surf. Sci.* **2010**, *257*, 887−898.
(53) Dufond, M. E.; Diouf, M. W.; Badie, C.; Laffon, C.; Parent, P.; Ferry, D.; Grosso, D.; Kools, J. C. S.; Elliott, S. D.; Santinacci, L. Quantifying the Extent of Ligand Incorporation and the Effect on Properties of TiO2 Thin Films Grown by Atomic Layer Deposition Using an Alkoxide or an Alkylamide. *Chem. Mater.* **2020**, *32*, 1393−1407.
(54) Kwon, S. J.; Song, H. S.; Im, H. B.; Nam, J. E.; Kang, J. K.; Hwang, T. S.; Yi, K. B. Preparationand Characterization of Rutile-Anatase Hybrid TiO_2 Thin Film by Hydrothermal Synthesis. *Clean Technol.* **2014**, *20*, 306−313.
(55) He, J.; Du, Y. e.; Bai, Y.; An, J.; Cai, X.; Chen, Y.; Wang, P.; Yang, X.; Feng, Q. Facile Formation of Anatase/Rutile TiO2 Nanocomposites with Enhanced Photocatalytic Activity. *Molecules* **2019**, *24*, 2996.
(56) Scarpelli, F.; Mastropietro, T. F.; Godbert, T. P. Mesoporous TiO2 Thin Films: State of the Art. *Titanium Dioxide - Material for a Sustainable Environment*; IntechOpen 2018. DOI: 10.5772/INTECHOPEN.74244.
(57) Javed, M. S.; Shah, S. S. A.; Najam, T.; Siyal, S. H.; Hussain, S.; Saleem, M.; Zhao, Z.; Mai, W. Achieving High-Energy Density and Superior Cyclic Stability in Flexible and Lightweight Pseudocapacitor through Synergic Effects of Binder-Free CoGa2O4 2D-Hexagonal Nanoplates. *Nano Energy* **2020**, *77*, No. 105276.
(58) Luan, F.; Wang, G.; Ling, Y.; Lu, X.; Wang, H.; Tong, Y.; Liu, X. X.; Li, Y. High Energy Density Asymmetric Supercapacitors with a Nickel Oxide Nanoflake Cathode and a 3D Reduced Graphene Oxide Anode. *Nanoscale* **2013**, *5*, 7984−7990.

https://doi.org/10.1021/acsomega.3c01676
ACS Omega 2023, 8, 17220−17233